

1
2
3
4
5
6
7
8
9
10
11
12
13
14
15
16
17
18
19
20
21
22
23
24
25
26
27
28
29
30
31
32
33
34
35
36
37
38
39
40
41

**Diapycnal mixing across the photic zone of the
NE-Atlantic**

**by Hans van Haren*, Corina P.D. Brussaard, Loes J. A.
Gerringa, Mathijs H. van Manen, Rob Middag,
Ruud Groenewegen**

Royal Netherlands Institute for Sea Research (NIOZ), P.O. Box 59, 1790 AB Den Burg,
the Netherlands.

*e-mail: hans.van.haren@nioz.nl

42 **Abstract.** Variable physical conditions such as vertical turbulent exchange, internal wave and
43 mesoscale eddy action, affect the availability of light and nutrients for phytoplankton
44 (unicellular algae) growth. It is hypothesized that changes in ocean temperature may affect
45 ocean vertical density stratification, which may hamper vertical exchange. In order to quantify
46 variations in physical conditions in the Northeast Atlantic Ocean, we sampled a latitudinal
47 transect along $17\pm 5^\circ\text{W}$ between 30 and 63°N in summer. A shipborne Conductivity-
48 Temperature-Depth CTD-instrumented package was used with a custom-made modification of
49 the pump-inlet to minimize detrimental effects of ship motions on its data. Thorpe-scale
50 analysis was used to establish turbulence values for the upper 500 m from 3 to 6 profiles
51 obtained in a short CTD-yoyo, 3 to 5 h after local sunrise. From south to north, average
52 temperature decreased together with stratification while turbulence values weakly increased or
53 remained constant. Vertical turbulent nutrient fluxes did not vary significantly with
54 stratification and latitude. This apparent lack of correspondence between turbulent mixing and
55 temperature is likely due to internal waves breaking (increased stratification can support more
56 internal waves), acting as a potential feed-back mechanism. As this feed-back mechanism
57 mediates potential physical environment changes in temperature, global surface ocean warming
58 may not affect the vertical nutrient fluxes to a large degree. We urge modelers to test this
59 deduction as it could imply that the future summer phytoplankton productivity in stratified
60 oligotrophic waters would experience little alterations in nutrient input from deeper waters.

61

62

63 **1 Introduction**

64 The physical environment is important for ocean life, including variations therein. For
65 example, the sun stores heat in the ocean with a stable vertical density stratification as result.
66 Generally, stratification hampers vertical turbulent exchange because of the required work
67 against (reduced) gravity before turbulence can take effect. It thus hampers a supply of nutrients
68 via a turbulent flux from deeper waters to the photic zone. However, stratification supports
69 internal waves, which (i) may move near-floating particles like phytoplankton (unicellular
70 algae) up- and down towards and away from the surface, and (ii) may induce enhanced
71 turbulence via vertical current differences (shear) resulting in internal waves breaking (Denman
72 and Gargett, 1983). Such changes in the physical environment are expected to affect the
73 availability of phytoplankton growth factors such as light and nutrients.

74 Climate models predict that global warming will reduce vertical mixing in the oceans (e.g.,
75 Sarmiento et al., 2004). Mathematical models on system stability suggest that reduced mixing
76 may generate chaos behaviour in phytoplankton production, thereby enhancing variability in
77 carbon export into the ocean interior (Huisman et al., 2006). However, none of these models
78 include potential feed-back systems like internal wave action or mesoscale eddy activity. From
79 observations in the relatively shallow North Sea it is known that the strong seasonal temperature
80 stratification is marginally stable, as it supports internal waves and shear to such extent that
81 sufficient nutrients are replenished from below to sustain the late-summer phytoplankton bloom
82 in the euphotic zone that became depleted of nutrients after the spring bloom (van Haren et al.,
83 1999). This challenges the current paradigm in climate models.

84 In this paper, the objective is to resolve the effect of vertical stratification and turbulent
85 mixing on nutrient supply to the euphotic zone of the open ocean. For this purpose, upper-500-
86 m-ocean shipborne Conductivity-Temperature-Depth CTD-observations were made in
87 association with those on dissolved inorganic nutrients during a survey along a transect in the
88 NE-Atlantic Ocean from mid-(30°) to high--(63°) latitudes in summer. Throughout the survey,
89 meteorological and sea-state conditions were favourable for adequate sampling and wind

90 speeds varied little between 5 and 10 m s⁻¹, independent of locations. All CTD-observations
91 were made far from lateral, continental boundaries and at least 1000 m vertically away from
92 bottom topography (i.e. far from internal-tide sources). The NE-Atlantic is characterized by
93 abundant (sub-)mesoscale eddies especially in the upper ocean (Charria et al., 2017) that
94 influence local plankton communities (Hernández- Hernández et al., 2020). The area also
95 shows continuous abundant internal wave activity away from topographic sources and sinks,
96 with the semidiurnal tide as a main source from below and atmospherically induced inertial
97 motions from above (e.g., van Haren, 2005; 2007). However, the sampled upper 500-m zone
98 transect is not known to demonstrate outstanding internal wave source variations. Previous
99 observations (van Haren, 2005) and Hibiya et al. (2007) have shown that a diurnal critical
100 latitude enhancement of near-inertial internal waves due to subharmonic instability only occurs
101 sharply between 25 and 30°N. The present observations are all made poleward of this range.
102 Likewise, the Henyey et al. (1986) model on latitudinal variation of internal wave energy and
103 turbulent mixing (Gregg et al., 2003) predicts changes by a factor of maximum 1.8 between
104 30° and 63°, but this value is relatively small compared with errors, typically a factor of 2 to 3,
105 in turbulence dissipation rate observations. Likewise, from the equal summertime
106 meteorological conditions little variation is expected in the generation of upper ocean near-
107 inertial internal waves. Naturally, other processes like interaction between internal waves and
108 mesoscale phenomena may be important locally, but these are expected to occur in a similar
109 fashion across the sampled ocean far away from boundaries. Thus, the sampled dataset is
110 considered adequate for a discussion on the variability of turbulence, stratification and vertical
111 turbulent nutrient fluxes with latitude.

112 The present research complements research based on photic zone (upper 100 m)
113 observations obtained along the same transect using a slowly descending turbulence
114 microstructure profiler next to CTD-sampling eight years earlier (Jurado et al., 2012). Their
115 data demonstrated a negligibly weak increase in turbulence values with significant decreases in
116 stratification going north. However, no nutrient data were presented and no turbulent nutrient

117 fluxes could be computed. In another summertime study (Mojica et al., 2016), macro-nutrient
118 concentrations indicated oligotrophic conditions along the same latitudinal transect but the
119 vertical gradients for the upper 200 m showed an increase from south to north. The present
120 observations go deeper to 500 m, also across the non-seasonal more permanent stratification.
121 Moreover, coinciding measurements were made of the distributions of macro-nutrients and
122 dissolved iron. This allows vertical turbulent nutrient fluxes to be computed. It leads to a
123 hypothesis concerning a physical feed-back mechanism that may control changes in
124 stratification.

125

126 **2 Materials and Methods**

127 Between 22 July and 16 August 2017, observations were made from the R/V Pelagia in the
128 Northeast Atlantic Ocean at stations along a transect from Iceland, starting around 60°N, to the
129 Canary Islands, ending at 30°N, (Fig. 1). The transect was roughly in meridional direction, with
130 stations along 17±5°W, all in the same time zone (UTC-1 h = local time LT). Full water-depth
131 Rosette bottle water sampling was performed at most stations.

132 Samples for dissolved inorganic macro-nutrients were filtered through 0.2 µm Acrodisc
133 filter and stored frozen in a high-density polyethylene pony-vial (nitrate, nitrite and phosphate)
134 or at 4°C (silicate) until analysis. Nutrients were analysed under temperature controlled
135 conditions using a QuAAtro Gas Segmented Continuous Flow Analyser. All measurements
136 were calibrated with standards diluted in low nutrient seawater in the salinity range of the
137 stations to ensure that analysis remained within the same ionic strength. Phosphate (PO₄),
138 nitrate plus nitrite (NO_x), were measured according to Murphy and Riley (1962) and Grasshoff
139 et al. (1983), respectively. Silicate was analysed using the procedure of Strickland and Parsons
140 (1968).

141 Absolute and relative precision were regularly determined for reasonably high
142 concentrations in an in-house standard. For phosphate, the standard deviation was 0.028 µM
143 (N = 30) for a concentration of 0.9 µM; Hence the relative precision was 3.1%. For nitrate, the

144 values were 0.14 μM ($N = 30$) for a concentration of 14.0 μM , so that the relative precision was
145 1.0%. For silicate, the values were 0.09 μM ($N = 15$) for a concentration of 21.0 μM , so that
146 the relative precision was 0.4%. The detection limits were 0.007, 0.012 and 0.008 μM , for
147 phosphate, nitrate and silicate, respectively.

148 For dissolved iron samples, the ultraclean “Pristine” sampling system for trace metals was
149 used (Rijkenberg et al., 2015). All bottles used for storage of reagents and samples were cleaned
150 according to an intensive three step cleaning protocol described by Middag et al. (2009).
151 Dissolved iron concentrations were measured shipboard using a Flow Injection—
152 Chemiluminescence method with preconcentration on iminodiacetic acid resin as described by
153 De Baar et al. (2008) and modified by Klunder et al. (2011). In order to validate the accuracy
154 of the system, standard reference seawater (SAFe) was measured regularly in triplicate
155 (Johnson et al. 1997).

156 At 19 out of 32 stations a yoyo consisting of 3 to 6 casts, totaling 88 casts, of electronic
157 CTD profiles was done to monitor the temperature-salinity variability and to establish turbulent
158 mixing values from 5 to 500 m below the ocean surface. For the yoyos a separate CTD was
159 used from the CTD -- ultraclean sampling system. The yoyo casts were made consecutively
160 and took between 1 and 2 hours per station. They were mostly obtained in the morning: at ten
161 stations between 6 and 8 LT, at eight stations between 8 and 10 LT, and at one station in the
162 afternoon, around noon. As the observations were made in summer, the latitudinal difference
163 in sunrise was 1.5 h between the northernmost (earlier sunrise) and southernmost stations. This
164 difference is taken into account and sampling times are referenced to time after local sunrise. It
165 is assumed that the stations sampled just after sunrise reflect the upper ocean conditions of (late-
166) nighttime cooling convection so that vertical near-homogeneity was at a maximum, and near-
167 surface stratification at a minimum, while the late morning and afternoon stations reflected
168 daytime stratifying near-surface conditions due to the stabilizing solar insolation.

169

170 **2.1 Instrumentation and modification**

171 Calibrated SeaBird 911plus CTDs were used. The CTD data were sampled at a rate of 24
172 Hz, whilst lowering the instrumental package at an average speed of 0.9 m s^{-1} . The yoyo CTD
173 data were processed using the standard procedures incorporated in the SBE-software, including
174 corrections for cell thermal mass (Lueck, 1990) using the parameter setting of Mensah et al.
175 (2009), sensor time-alignment and vertical bin-averaging over 0.33 m. All other analyses were
176 performed using Conservative Temperature (Θ), Absolute Salinity S_A and potential density
177 anomalies σ_θ , with 1000 kg m^{-3} subtracted from total density and referenced to the surface for
178 pressure corrections as vertical profiles were only analyzed shallower than 600 m, using the
179 Gibbs SeaWater-software (IOC, SCOR, IAPSO, 2010).

180 Observations were made with the yoyo CTD upright rather than horizontal in a lead-
181 weighted frame without water samplers to minimize artificial turbulent overturning. Variable
182 speeds of the flow passing the temperature and conductivity sensors will cause artificial
183 temperature and thus apparent turbulent overturning, noticeable in near-homogeneous waters
184 such as found near the surface during nighttime convection. To eliminate variable flow speeds,
185 a custom-made assembly with pump in- and outlet tubes and tube-ends of exactly the same
186 diameter was mounted to the CTD as described in van Haren and Laan (2016). This reduces
187 frictional temperature effects of typically $\pm 0.5 \text{ mK}$ due to fluctuations in pump speed of ± 0.5
188 m s^{-1} when standard SBE-tubing is used (Appendix A1). The effective removal of the artificial
189 temperature effects using the custom-made assembly is demonstrated in Fig. 2, in which surface
190 wave action via ship motion is visible in the CTD-pressure record, but not in its temperature
191 variations record. For example, at station 32 the CTD was lowered in moderate sea state
192 conditions with surface waves of maximum 2 m crest-trough. The surface waves are recorded
193 by pressure variations as a result of ship motions (Fig. 2a). In the upper 35 m near the surface,
194 the waters were partially unstable and partially near-homogeneous, with temperature variations
195 well within $\pm 0.5 \text{ mK}$ and high-frequency variations $O(0.1) \text{ mK}$ (Fig. 2b). The ΔT -variations
196 did not vary with the surface wave periodicity of about 10 s. No correlation was found between
197 data in Fig. 2b and Fig. 2a. This effective removal of ship motion in CTD-temperature data is

198 confirmed for the entire 500 m depth-range in average spectral information (Fig. 2c-e). In the
 199 power spectra, the pressure gradient $dp/dt \sim$ CTD-velocity shows a clear peak around 0.1 cps,
 200 short for cycles per s, which correspond to a period of 10 s. Such a peak is absent in both spectra
 201 of temperature T and density anomaly referenced to the surface σ_θ . The correlation between
 202 dp/dt and T is not significantly different from zero (Fig. 2d,e). With conventional tubing and
 203 tube-ends, the surface wave variations would show in such ΔT -graph (van Haren and Laan,
 204 2016). Without the effects of ship motions, considerably less corrections need to be applied for
 205 turbulence calculations (see below).

206

207 **2.2 Ocean turbulence calculation**

208 Turbulence is quantified using the analysis method by Thorpe (1977) on potential density
 209 inversions of less dense water below a layer of denser water in a vertical (z) profile. Such
 210 inversions are interpreted as turbulent overturns of mechanical energy mixing. Vertical
 211 turbulent kinetic energy dissipation rate (ε) is a measure of the amount of kinetic energy put in
 212 a system for turbulent mixing. It is proportional to the magnitude of turbulent diapycnal flux
 213 (of potential density) $|K_z d\sigma_\theta/dz|$. In practice it is determined by calculating overturning scales
 214 with magnitude $|d|$, just like turbulent eddy diffusivity (K_z). The vertical potential density
 215 stratification is indicated by $d\sigma_\theta/dz$. The turbulent overturning scales are obtained after
 216 reordering the measured profile $\sigma_\theta(z)$, which may contain inversions, into a stable monotonic
 217 profile $\sigma_\theta(z_s)$ without inversions (Thorpe, 1977). After comparing raw and reordered profiles,
 218 displacements $d = \min(|z-z_s|) \cdot \text{sgn}(z-z_s)$ are calculated that generate the stable profile. Then,
 219 using root-mean-square displacement value $L_T = \text{rms}(d)$ computed over certain vertical scales
 220 (see below),

$$221 \quad \varepsilon = 0.64L_T^2 N^3 \quad [\text{m}^2\text{s}^{-3}], \quad (1)$$

222 where $N = \{-g/\rho(d\sigma_\theta(z_s)/dz)\}^{1/2}$ denotes the buoyancy frequency (\sim square-root of stratification
 223 as is clear from the equation) computed from the reordered profile. Here, g is the acceleration
 224 of gravity and $\rho = 1027 \text{ kg m}^{-3}$ denotes the reference density. We like to note, following

225 previous warnings by, e.g., Gill (1982) and King et al. (2012), that our definition of N is a
 226 practical one, which should not be used for data from deeper waters. For deeper waters, density
 227 should be referenced to a local pressure reference level, which effectively implies the use of the
 228 exact definition for buoyancy frequency as formulated, e.g., by Gill (1982): $\{-g/\rho(dp/dz +$
 229 $gp/c_s^2)\}^{1/2}$, where c_s is the speed of sound reflecting pressure-compressibility effects. Our
 230 ‘surface waters’ N computed over reordered profiles only negligibly deviates from above exact
 231 N and corresponds with N computed from raw profiles over a typical vertical length-scale of
 232 $\Delta z = 100$ m. This Δz represents the scales of large internal waves that are supported by the
 233 density stratification and of the largest turbulent overturns.

234 The numerical constant of 0.64 in (1) follows from empirically relating the overturning scale
 235 magnitude with the Ozmidov scale L_O of largest possible turbulent overturn in a stratified flow:
 236 $(L_O/L_T) = 0.8$ (Dillon, 1982), a mean coefficient value from many realizations. Using $K_z = \Gamma \epsilon N^{-1}$
 237 2 and a mean mixing efficiency coefficient of $\Gamma = 0.2$ for the conversion of kinetic into potential
 238 energy for ocean observations that are suitably averaged over all relevant turbulent overturning
 239 scales of the mix of shear-, current differences, and convective, buoyancy driven, turbulent
 240 overturning in large Reynolds number flow conditions (e.g., Osborn, 1980; Oakey, 1982;
 241 Ferron et al., 1998; Gregg et al., 2018), we find,

$$242 \quad K_z = 0.128 L_T^2 N \quad [m^2 s^{-1}]. \quad (2)$$

243 This parametrization is also valid for the upper ocean, as has been shown extensively by Oakey
 244 (1982) and recently confirmed by Gregg et al. (2018). The inference is that the upper ocean
 245 may be weakly stratified at times, but stratification and turbulence vary considerably with time
 246 and space. Sufficient averaging collapses coefficients to the mean values given above. This is
 247 confirmed in recent numerical modeling by Portwood et al. (2019).

248 As K_z is a mechanical turbulence coefficient it is not property-dependent like a molecular
 249 diffusion coefficient that is about 100-fold different for temperature compared to salinity. K_z is
 250 thus the same for all turbulent transport calculations no matter what gradient of what property.

251 For example, the vertical downgradient turbulent flux of dissolved iron transporting from iron-
252 rich deeper waters upwards into the euphotic zone is computed as $-K_z d(\text{DFe})/dz$.

253 According to Thorpe (1977), results from (1) and (2) are only useful after averaging over
254 the size of a turbulent overturn instead of using single displacements. Here, rms-displacement
255 values L_T are not determined over individual overturns, as in Dillon (1982), but over 7 m
256 vertical intervals (equivalent to about 200 raw data samples) that just exceed average L_0 . This
257 avoids the complex distinction of smaller overturns in larger ones and allows the use of a single
258 length scale of averaging. As a criterion for determining overturns we only used those data of
259 which the absolute value of difference with the local reordered value exceeds a threshold of
260 $7 \times 10^{-5} \text{ kg m}^{-3}$, which comes from standard deviations of the potential density profiles in near-
261 homogeneous layers over 1-m intervals and which corresponds to noise-variational amplitudes
262 of $1.4 \times 10^{-4} \text{ kg m}^{-3}$ in raw data (e.g., Galbraith and Kelley, 1996; Stansfield et al., 2001; Gargett
263 and Garner, 2008). Vertically averaged turbulence values, short for averaged ε - and K_z -values
264 from (1) and (2), can be calculated to within an error of a factor of two to three, approximately.
265 As will be demonstrated below, this is considerably less spread in values than the natural
266 turbulence values variability over typically four orders of magnitude at a given position and
267 depth in the ocean (e.g., Gregg, 1989).

268

269 **3 Results**

270 **3.1 Physical parameters**

271 An early morning vertical profile of density anomaly in the upper 500 m at a northern
272 station (Fig. 3a) is characterized by a near-homogeneous layer of about 15 to 40 m, which is
273 above a layer of relatively strong stratification and a smooth moderate stratification deeper
274 below. In the near-homogeneous upper layer, in this example $z > -30$ m, relatively large
275 turbulent overturn displacements can be found of $d = \pm 20$ m (Fig. 3b): so called large density
276 inversions. In this paper we conventionally define ‘mixed layer depth’ as the depth at which the
277 temperature difference with respect to the surface is 0.5°C (Jurado et al., 2012). We note that

278 this actually more represents the ‘mixing layer depth’ and the reordered profile shows non-zero
279 stratification. If the mixed-layer-depth definition would have been applying a temperature
280 difference of, e.g., 0.001°C on the reordered profile, its value would average about 5 m, much
281 less than using the present and more common, conventional definition applying a temperature
282 difference of 0.5°C. We thus present turbulence results for this commonly defined ‘mixed layer’
283 with caution, whilst observing their consistency with the results from deeper down, as presented
284 below. For $-200 < z < -30$ m, large turbulent overturns are few and far between. Turbulence
285 dissipation rate (Fig. 3c) and eddy diffusivity (Fig. 3d) are characterized by relatively small
286 displacement sizes of less than 5 m. For $z < -200$ m, displacement values weakly increase with
287 depth, together with stratification ($\sim N^2$; Fig. 3e). Between $-30 < z < 0$ m, turbulence dissipation
288 rate values between our minimum detectable level 10^{-11} and $>10^{-8} \text{ m}^2 \text{ s}^{-3}$ are similar to those
289 found by others, using microstructure profilers (e.g., Oakey, 1982; Gregg, 1989), lowered
290 acoustic Doppler current profiler or CTD-Thorpe scale analysis (e.g., Ferron et al., 1998; Walter
291 et al., 2005; Kunze et al., 2006). Here, eddy diffusivities are found between our minimum
292 detectable 2×10^{-5} and $3 \times 10^{-3} \text{ m}^2 \text{ s}^{-1}$ and these values compare with previous near-surface results
293 (Denman and Gargett, 1983). The relatively small $|d| < 5$ m displacements (Fig. 3b) are genuine
294 turbulent overturns, and they resemble ‘Rankine vortices’, a common model of cyclones (van
295 Haren and Gostiaux, 2014), as may be best visible in this example in the large turbulent overturn
296 near the surface. The occasional erratic appearance in individual profiles, sometimes still visible
297 in the ten-profile means, reflects smaller overturns in larger ones.

298 A mid-morning profile at a southern station shows different characteristics (Fig. 4),
299 although 500 m vertically averaged turbulence values are similar to within 10% of those of the
300 northern station. This 10% variation is well within the error bounds of about a factor of two. At
301 this southern station, the near-surface layer is stably stratifying (Fig. 4a) and displays few
302 overturning displacements (Fig. 4b), while the interior demonstrates rarer but occasional
303 intense turbulent overturning (at $z = -160$ m in Fig. 4), presumably due to internal wave

304 breaking. At greater depths, stratification ($\sim N^2$; Fig. 4e) weakly decreases, together with ϵ (Fig.
305 4c) and K_z (Fig. 4d).

306 Latitudinal overviews are given in Fig. 5 for: Average values over the upper $z > -15$ m,
307 which covers the diurnal mainly convective turbulent mixing range from the surface and under
308 the cautionary note that these waters are weakly, but measurably stratified, average values
309 between $-100 < z < -25$ m, which covers the seasonal strong stratification, and average values
310 between $-500 < z < -100$ m, which covers the more permanent moderate stratification. Noting
311 that all panels have a vertical axis representing a logarithmic scale, variations over nearly four
312 orders of magnitude in turbulence dissipation rate (Fig. 5a) and eddy diffusivity (Fig. 5b) are
313 observed between casts at the same station. This variation in magnitude is typically found in
314 near-surface open-ocean turbulence microstructure profiles (e.g., Oakey, 1982). Still,
315 considerable variability over about two orders of magnitude is observed between the averages
316 from the different stations. This variation in station- and vertical averages far exceeds the
317 instrumental error bounds of a factor of two (0.3 on a log-scale), and thus reveals local
318 variability. The turbulence processes occur ‘intermittently’.

319 The observed variability over two orders of magnitude between yoyo-casts at a single
320 station may be due to active convective overturning during early morning in the near-
321 homogeneous upper layer, or due to internal wave breaking and sub-mesoscale variability
322 deeper down. Despite the large variability at stations, trends are visible between stations in the
323 upper 100 m over the 33° latitudinal range going poleward: Buoyancy frequency (\sim square root
324 of stratification) steadily decreases significantly (p -value < 0.05) given the spread of values at
325 given stations, with the notion that near-surface ($-15 < z < 0$ m) values show the same latitudinal
326 trend as deeper-down-values across a larger spread of values, while turbulence values vary
327 insignificantly with latitude as they remain the same or weakly increase by about half an order
328 of magnitude (about a factor of 3). At a given depth range, turbulence dissipation rates roughly
329 follow a log-normal distribution with standard deviations well exceeding half an order of
330 magnitude. The comparison of latitudinal variations with the (log-normal) distribution is
331 declared insignificant with $p > 0.05$ when the mean values are found within 2 standard

332 deviations (see Appendix A2). This is not only performed for turbulence dissipation rate, but
333 also for other quantities. The trends suggest only marginally larger turbulence going poleward,
334 which is possibly due to larger cooling from above and larger internal wave breaking deeper
335 down. It is noted that the results are somewhat biased by the sampling scheme, which changed
336 from 3 to 4 h after sunrise sampling at high latitudes to 4 to 5 h after sunrise sampling at lower
337 latitudes, see the sampling hours after local sunrise in (Fig. 5d). Its effect is difficult to quantify,
338 but should not show up in turbulence values from deeper down ($-500 < z < -100$ m).

339 Between $-500 < z < -100$ m, no clear significant trend with latitude is visible in the
340 turbulence values (Fig. 5a,b), although $[K_z]$ weakly increases with increasing latitude at all
341 levels between $-500 < z < 0$ m, while buoyancy frequency significantly decreases (Fig. 5c). The
342 data from well-stratified waters deeper down thus show the same latitudinal trend as the
343 observations from the near-surface layers, even though the latter are less well determined
344 because of the weak stratification. Our turbulence values from CTD-data also confirm previous
345 results by Jurado et al. (2012) who made microstructure profiler observations from the upper z
346 > -100 m along the same transect. Their results showed turbulence values remain unchanged
347 over 30° latitude or increase by at most one order of magnitude, depending on depth level. Their
348 ‘mixed’ layer ($z > -25$ m) turbulence values are similar to our $z > -15$ m values and half to one
349 order of magnitude larger than the present deeper observations. The slight discrepancy in values
350 averaged over $z > -25$ m may point at either i) a low bias due to a too strict criterion of accepting
351 density variations for reordering applied here, or ii) a high bias of the ~ 10 -m largest overturns
352 having similar velocity scales (of about 0.05 m s^{-1}) as their 0.1 m s^{-1} slowly descending SCAMP
353 microstructure profiler. At greater depths, $-500 < z < -100$ m, it is seen in the present
354 observations that the spread in turbulence values over four orders of magnitude at a particular
355 station is also large. This spread in values suggests that dominant turbulence processes show
356 similar intermittency in weakly (at high-latitudes $N \approx 10^{-2.5} \text{ s}^{-1}$) and moderately (at mid-latitudes
357 $N \approx 10^{-2.2} \text{ s}^{-1}$) stratified waters, respectively, for the given resolution of the instrumentation.

358 Mean values of N are larger by half an order of magnitude in the seasonal pycnocline (found
359 in the range $-100 < z < -25$ m) than those near the surface and in the more permanent

360 stratification below (Fig. 5). Such local vertical variations in N have the same range of variation
361 as observed horizontally across latitudes $[30, 63]^{\circ}$ per depth level.

362

363 **3.2 Nutrient distributions and fluxes**

364 Vertical profiles of macro-nutrients generally resemble those of density anomaly in the
365 upper $z > -500$ m (Fig. 6). In the south, low macro-nutrient values are generally distributed over
366 a somewhat larger near-surface mixed layer. The mixed layer depth, at which temperature
367 differed by 0.5°C from the surface (Jurado et al., 2012), varies between about 20 and 30 m on
368 the southern end of the transect and weakly becomes shallower with latitude (Fig. 7a). This
369 weak trend may be expected from the summertime wind conditions that also barely vary with
370 latitude (Fig. 7b,c). In contrast, the euphotic zone, defined as the depth of the 0.1% irradiance
371 penetration level (Mojica et al., 2015), demonstrates a clear latitudinal trend decreasing from
372 about 150 to 50 m (Fig. 7a). For $z < -100$ m below the seasonal stratification, vertical gradients
373 of macro-nutrients are large (Fig. 6b-d). Macro-nutrient values become approximately
374 independent of latitude at depths below $z < -500$ m. Dissolved iron profiles differ from macro-
375 nutrient profiles, notably in the upper layer near the surface (Fig. 6a). At some southern stations,
376 dissolved iron and to a lesser extent also phosphate, have relatively high concentrations closest
377 to the surface. These near-surface concentration increases suggest atmospheric sources, most
378 likely Saharan dust deposition (e.g., Rijkenberg et al., 2012).

379 As a function of latitude in the near-surface ‘mixed’ layer (Fig. 8), the vertical turbulent
380 fluxes of phosphate (representing the macro-nutrients, for graphical reasons, see the similarity
381 in profiles in Fig.6b-d) are found constant or insignificantly ($p > 0.05$) increasing (Fig. 8d).
382 Here, the mean eddy diffusivity values for the near-surface layer as presented in Fig. 5 are used
383 for computing the fluxes. It is noted that in this layer turbulent overturning (Figs 3b, 4b) is
384 larger and nutrients are mainly depleted (Fig. 6), except when replenished from atmospheric
385 sources in which case gradients reverse sign as in most DFe-profiles. Hereby, lateral diffusion
386 is not considered important. Nonetheless, macro-nutrients are seen to increase significantly
387 towards higher latitudes (Fig. 8b). We note that the vertical gradients in Fig. 8c, in which only

388 downgradient values are plotted, are very weak in general within the standard deviation of
389 measurements. The results in Fig. 8d are thus merely indicative, but they are consistent with
390 the results from deeper down presented below.

391 More importantly, the significant vertical turbulent fluxes of nutrients across the seasonal
392 pycnocline (Fig. 9) are found ambiguously or statistically independently varying with latitude
393 (Fig. 9d). Likewise, the vertical turbulent fluxes of dissolved iron and phosphate are marginally
394 constant with latitude across the more permanent stratification deeper down (Fig. 10). Nitrate
395 fluxes show the same latitudinal trend, with values around 10^{-6} mmol m⁻² s⁻¹. Overall, the
396 vertical turbulent nutrient fluxes across the seasonal and more permanent stratification resemble
397 those of the physical vertical turbulent mass flux, which is equivalent to the distribution of
398 turbulence dissipation rate and which is latitude-invariant (Fig. 5a).

399

400 **4 Discussion**

401 Practically, the upright positioning CTD while using an adaptation consisting of a custom-
402 made equal-surface inlet worked well to minimize ship-motion effects on variable flow-
403 imposed temperature variations. This improved calculated turbulence values from CTD-
404 observations in general and in near-homogeneous layers in particular. The indirect comparison
405 with turbulence values determined from previous microstructure profiler observations along the
406 same transect (Jurado et al., 2012) confirms the same trends, although occasionally turbulence
407 values were lower (to one order of magnitude in the present study). This difference in values
408 may be due to the time-lapse of 8 years between the observations, but more likely it is due to
409 inaccuracies in one or both methods. It is noted that any ocean turbulence observations cannot
410 be made better than to within a factor of two (Oakey, pers. comm.). In that respect, the standard
411 CTD with the here presented adaptation is a cheaper solution than additional microstructure
412 profiler observations. Although the general understanding, mainly amongst modellers, is that
413 the Thorpe length method overestimates diffusivity (e.g., Scotti, 2015; Mater and
414 Venayagamoorthy, 2015), this view is not shared amongst ocean observers (e.g., Gregg et al.,

415 2018). In the large parameter space of the high Reynolds number environment of the ocean,
416 turbulence properties vary constantly, with an interminglement of convection and shear-
417 induced turbulence at various levels. Given sufficient averaging, and adequate mean value
418 parametrization, the Thorpe length method is not observed to overestimate diffusivity. This
419 property of adequate and sufficient averaging yields similar mean parameter values in recent
420 modelling results estimating a mixing coefficient near the classical bound of 0.2 in stationary
421 flows for a wide range of conditions (Portwood et al., 2019). It is noted that diffusivity always
422 requires knowledge of stratification to obtain a turbulent flux, and it is better to consider
423 turbulence dissipation rate for intercomparison purposes. Nevertheless, future research may
424 perform a more extensive comparison between Thorpe scale analysis data and deeper
425 microstructure profiler data.

426 While our turbulence values are roughly similar to those of others transecting the NE-
427 Atlantic over the entire water depth (Walter et al., 2005; Kunze et al., 2006), the focus in the
428 present paper is on the upper 500 m because of its importance for upper-ocean marine biology.
429 Our study demonstrates a significant decrease of stratification with increasing latitude and
430 decreasing temperature that, however, does not lead to significant variation in turbulence values
431 and vertical turbulent fluxes. Our direct estimates of the turbulent flux of nitrate into the
432 euphotic zone are one to two orders of magnitude less than the previously estimated rate of
433 nitrate uptake for the summer period. Our turbulent flux of nitrate values are of the same order
434 of magnitude as reported by others (Cyr et al., 2015 and references therein). In particular, the
435 Martin et al. (2010) study in the Northeast Atlantic Ocean (at 49°N, 16°W) reported similar
436 vertical nutrient fluxes during summer, which provides confidence in the methods used. The
437 same authors reported that the vertical nitrate flux into the euphotic zone was much lower than
438 the rate of nitrate uptake at the time. To determine these nitrate uptake rates, they spiked water
439 samples with a minimum of 0.5 μM nitrate, representing $\sim 10\%$ of the ambient nitrate
440 concentration. In our study area, the ambient nitrate concentrations in the euphotic zone were
441 much lower (see also Mojica et al., 2015), implying a higher relative importance of nitrate input
442 to the overall uptake demand. Still, primary productivity in the oligotrophic euphotic zone, as

443 well as in the high latitude Atlantic, is mainly fueled by recycling (e.g., Gaul et al., 1999;
444 Achterberg et al., 2020) and the supply of new nutrients by turbulent fluxes, however small,
445 provides a welcome addition. Besides nutrient input resulting from vertical turbulent fluxes,
446 there is a role for latitudinal differences through the supply of nutrients by deep mixing events,
447 and depending on the location, also potential upwelling and lateral transport events.

448 We suggest that internal waves may drive the feed-back mechanism, participating in the
449 subtle balance between destabilizing shear and stable (re)stratification. Molecular diffusivity of
450 heat is about $10^{-7} \text{ m}^2 \text{ s}^{-1}$ in seawater, and nearly always smaller than turbulent diffusivity in the
451 ocean. The average values of K_z during our study were typically 100 to 1000 times larger than
452 molecular diffusivity, which implies turbulent diapycnal mixing drives vertical fluxes despite
453 the relatively slow turbulence compared to surface wave breaking. Depending on the gradient
454 of a substance like nutrients or matter, the relatively slow turbulence may not necessarily
455 provide weak fluxes $-K_z d(\text{substance})/dz$ into the photic zone. In the central North Sea, a
456 relatively low mean value of $K_z = 2 \times 10^{-5} \text{ m}^2 \text{ s}^{-1}$ comparable to values over the seasonal
457 pycnocline here, was found sufficient to supply nutrients across the strong summer pycnocline
458 to sustain the entire late-summer phytoplankton bloom in near-surface waters and to warm up
459 the near-bottom waters by some 3°C over the period of seasonal stratification (van Haren et al.,
460 1999). There, the turbulent exchange was driven by a combination of tidal currents modified
461 by the stratification, shear by inertial motions driven by the Coriolis force (inertial shear) and
462 internal wave breaking. Such drivers are also known to occur in the open ocean, although to an
463 unknown extent.

464 The here observed (lack of) latitudinal trends of ϵ , K_z and N yield approximately the same
465 information as the vertical trends in these parameters at all stations. In the vertical for $z < -200$
466 m, turbulence values of ϵ and K_z weakly vary with stratification. This is perhaps unexpected
467 and contrary to the common belief of stratification hampering vertical turbulent exchange of
468 matter including nutrients. It is less surprising when considering that increasing stratification is
469 able to support larger shear. Known sources of destabilizing shear include near-inertial internal

470 waves of which the vertical length-scale is relatively small compared to other internal waves,
471 including internal tides (LeBlond and Mysak, 1978).

472 The dominance of inertial shear over shear by internal tidal motions (internal tide shear),
473 together with larger energy in the internal tidal waves, has been observed in the open-ocean,
474 e.g. in the Irminger Sea around 60°N (van Haren, 2007). The frequent atmospheric disturbances
475 in that area generate inertial motions and dominant inertial shear. Internal tides have larger
476 amplitudes but due to much larger length scales they generate weaker shear, than inertial
477 motions. Small-scale internal waves near the buoyancy frequency are abundant and may break
478 sparsely in the ocean interior outside regions of topographic influence. However, larger
479 destabilizing shear requires larger stable stratification to attain a subtle balance of ‘constant’
480 marginal stability (van Haren et al., 1999). Not only storms but all geostrophic adjustments,
481 such as frontal collapse, may generate inertial wave shear also at low latitudes (Alford and
482 Gregg, 2001), so that overall latitudinal dependence may be negligible. If shear-induced
483 turbulence in the upper ocean is dominant it may thus be latitudinally independent (shallow
484 observations by Jurado et al., 2012; deeper observations in present study). There are no
485 indications that the overall open ocean internal wave field and (sub)mesoscale activities are
486 energetically much different across the mid-latitudes. If internal tide sources would have
487 dominated our observations, clear differences in turbulence dissipation rates would have been
488 found at our station near 48 °N (near the Porcupine Bank), for example, compared with those
489 at other stations.

490 Summarizing, our study infers that vertical nutrient fluxes did not vary significantly with
491 latitude and stratification. This suggests that predicted changes in the physical environment due
492 to global ocean warming have little effect on vertical turbulent exchange. Supposing that
493 enhanced warming leads to more stable stratification, more internal waves can be supported
494 (LeBlond and Mysak, 1978), which upon breaking can maintain the extent of vertical turbulent
495 exchange and thereby, for example, vertical nutrient fluxes. We thus hypothesize that, from a
496 physical environment perspective, in stratified oligotrophic waters the nutrient input from
497 deeper waters and corresponding summer phytoplankton productivity and growth are not

498 expected to change (much) with future global warming. We invite future observations and
499 numerical modelling to further investigate this suggestion and associated feed-back
500 mechanisms such as internal wave breaking.

501

502 *Data availability.* Data are available under doi/10.25850/nioz/7b.b.lb.

503

504 *Author contributions.* HvH analysed the data and drafted the paper. CPDB coordinated the
505 cruise. RM, MHvM and CPDB provided the nutrient and iron data. LJAG initiated the link of
506 disciplines in this study and stored the data sets. RG handled and operated the CTD-systems.
507 All authors contributed to the scientific discussion and edited the manuscript. All authors have
508 read and agreed to the published version of the manuscript.

509

510 *Competing interests.* The authors declare that they have no conflict of interest.

511

512 *Acknowledgements.* We thank the master and crew of the R/V Pelagia for their pleasant
513 contributions to the sea-operations. J. van Heerwaarden and R. Bakker made the CTD-
514 modification. We much appreciated the critical comments of the reviewers.

515

516

517 Modification of CTD pump-tubing to minimize RAM-effects

518 The unique pump system on SeaBird Electronics (SBE) CTDs, foremost on their high-
519 precision full ocean depth shipborne and cable-lowered SBE911, minimizes the effects of flow
520 variations (and inversions) past its T-C sensors (SeaBird, 2012). This reduction in flow
521 variation is important because the T-sensor has a slower response than the C-sensor. As data
522 from the latter are highly temperature dependent, besides being pressure dependent, the precise
523 matching of all three sensors is crucial for establishing proper salinity and density
524 measurements, especially across rapid changes in any of the parameters. As flow past the T-
525 sensor causes higher measurement values due to friction at the sensor tip, flow-fluctuations are
526 to be avoided as they create artificial T-variations of about 1 mK s m^{-1} (Larson and Pedersen,
527 1996).

528 However, while the pump itself is one thing, its tubing needs careful mounting as well, with
529 in- and outlet at the same depth level (Sea-Bird, 2012). This is to prevent ram pressure $P = \rho U^2$,
530 for density ρ and flow speed U . Unfortunately, the SBE-manual shows tubing of different
531 diameters, for in- and outlet. Different diameter tubing leads to velocity fluctuations of $\pm 0.5 \text{ m}$
532 s^{-1} past the T-sensor, as was concluded from a simple experiment by van Haren and Laan
533 (2016). The flow speed variations induce temperature variations of $\pm 0.5 \text{ mK}$ and are mainly
534 detectable in weakly stratified waters such as in the deep ocean, but also near the surface as
535 observed in the present data. Using tubes of the same diameter opening remedied most of the
536 effect, but only if the surface of the tube-opening is perpendicular to the main CT-motion as in
537 a vertically mounted CTD. If it is parallel to the main motion as in a horizontally mounted CTD,
538 the effect was found to be adverse. The make-shift onboard experiment in van Haren and Laan
539 (2016) has now been cast into a better design (Fig. A1), of which the first results are presented
540 in this paper.

541

542 PDFs of vertically averaged dissipation rate in comparison with latitudinal trends

543 Ocean turbulence dissipation rate generally tends to a nearly log-normal distribution (e.g.,
544 Pearson and Fox-Kemper, 2018), so that the probability density function (PDF) of the logarithm
545 of ε -values is normally distributed and can be described by the first two moments, the mean
546 and its standard deviation. It is seen in Fig. A2a that the overall distribution of all present data
547 indeed approaches lognormality, despite the relatively large length-scale used in the
548 computations (cf., Yamazaki and Lueck, 1990). When the data are split into the three depth
549 levels as in Fig. 5a, it is seen that ε in the upper $z > -15$ m layer is not log-normally distributed
550 due to a few outlying high values confirming an ocean state dominated by a few turbulence
551 bursts (Moum and Rippeth, 2009), whereas ε in the deeper more stratified layers is nearly log-
552 normally distributed.

553 When we compare the mean and standard deviations of the distributions with the extreme
554 values of the latitudinal trends as computed for Fig. 5a it is seen that for none of the three depth
555 levels the extreme values are found outside one standard deviation from the mean value. In fact,
556 for deeper stratified waters the extreme values of the trends are found very close to the mean
557 value. It is concluded that the mean dissipation rate does not show a significant trend with
558 latitude, at all depth levels. The same exercise yields extreme buoyancy frequency values lying
559 outside one standard deviation from the mean values for well-stratified waters, from which we
560 conclude that stratification significantly decreases with latitude. This is inferable from Fig. 5c
561 by investigating the spread of mean values around the trend line.

562

563 **References**

- 564 Alford, M. H. and Gregg, M. C.: Near-inertial mixing: Modulation of shear, strain and
565 microstructure at low latitude, *J. Geophys. Res.*, 106, 16,947-16,968, 2001.
- 566 Achterberg, E. P.: Trace element biogeochemistry in the high latitude North Atlantic Ocean:
567 seasonal variations and volcanic inputs, *Glob. Biogeochem. Cycl.* in press, doi:
568 10.1029/2020GB006674, 2020.
- 569 Charria, G., Theetten, S., Vandermeirsch, F., Yelekçi, Ö and Audiffren, N.: Interannual
570 evolution of (sub)mesoscale dynamics in the Bay of Biscay, *Ocean Sci.*, 13, 777-797, 2017.
- 571 Cyr, F., Bourgault, D., Galbraith, P. S. and Gosselin, M.: Turbulent nitrate fluxes in the Lower
572 St. Lawrence Estuary, Canada, *J. Geophys. Res.*, 120, 2308-2330,
573 doi:10.1002/2014JC010272, 2015.
- 574 De Baar, H. J. W. et al.: Titan: A new facility for ultraclean sampling of trace elements and
575 isotopes in the deep oceans in the international Geotraces program, *Mar. Chem.*, 111, 4-21,
576 2008.
- 577 Denman, K. L. and Gargett, A. E.: Time and space scales of vertical mixing and advection of
578 phytoplankton in the upper ocean, *Limnol. Oceanogr.*, 28, 801-815, 1983.
- 579 Dillon, T. M.: Vertical overturns: A comparison of Thorpe and Ozmidov length scales, *J.*
580 *Geophys. Res.*, 87, 9601-9613, 1982.
- 581 Ferron, B., Mercier, H., Speer, K., Gargett, A. and Polzin, K.: Mixing in the Romanche Fracture
582 Zone, *J. Phys. Oceanogr.*, 28, 1929-1945, 1998.
- 583 Galbraith, P. S. and Kelley, D. E.: Identifying overturns in CTD profiles, *J. Atmos. Oc.*
584 *Technol.*, 13, 688-702, 1996.
- 585 Gargett, A. and Garner, T.: Determining Thorpe scales from ship-lowered CTD density
586 profiles, *J. Atmos. Oc. Technol.*, 25, 1657-1670, 2008.
- 587 Gaul, W., Antia, A. N. and Koeve, W.: Microzooplankton grazing and nitrogen supply of
588 phytoplankton growth in the temperate and subtropical northeast Atlantic, *Mar. Ecol. Progr.*
589 *Ser.*, 189, 93-104, 1999.
- 590 Gill, A. E.: *Atmosphere-Ocean Dynamics*, Academic Press, Orlando, FL, USA, 662 pp, 1982.

591 Grasshoff, K., Kremling, K. and Ehrhardt, M.: Methods of seawater analysis, Verlag
592 Chemie GmbH, Weinheim, 419 pp, 1983.

593 Gregg, M. C.: Scaling turbulent dissipation in the thermocline, *J. Geophys. Res.*, 94, 9686-
594 9698, 1989.

595 Gregg, M. C., Sanford, T. B. and Winkel, D. P.: Reduced mixing from the breaking of internal
596 waves in equatorial waters, *Nature*, 422, 513-515, 2003.

597 Gregg, M. C., D'Asaro, E. A., Riley, J. J. and Kunze, E.: Mixing efficiency in the ocean, *Ann.*
598 *Rev. Mar. Sci.*, 10, 443-473, 2018.

599 Henyey, F. S., Wright, J. and Flatte, S. M.: Energy and action flow through the internal wave
600 field - an eikonal approach, *J. Geophys. Res.*, 91, 8487-8495, 1986.

601 Hernández-Hernández, N. et al.: Drivers of plankton distribution across mesoscale eddies at
602 submesoscale range, *Front. Mar. Sci.*, 7, 667, doi:10.3389/fmars.2020.00667, 2020.

603 Hibiya T., Nagasawa, M. and Niwa, Y.: Latitudinal dependence of diapycnal diffusivity in the
604 thermocline observed using a microstructure profiler, *Geophys. Res. Lett.*, 34, L24602,
605 2007.

606 Huisman, J., Pham Thi, N. N., Karl, D. M. and Sommeijer, B.: Reduced mixing generates
607 oscillations and chaos in the oceanic deep chlorophyll maximum, *Nature*, 439, 322-325,
608 2006.

609 Jurado, E., van der Woerd, H. J. and Dijkstra, H. A.: Microstructure measurements along a
610 quasi-meridional transect in the northeastern Atlantic Ocean, *J. Geophys. Res.*, 117,
611 C04016, doi:10.1029/2011JC07137, 2012.

612 IOC, SCOR, IAPSO: The international thermodynamic equation of seawater – 2010:
613 Calculation and use of thermodynamic properties, Intergovernmental Oceanographic
614 Commission, Manuals and Guides No. 56, UNESCO, Paris, France, 196 pp, 2010.

615 Johnson, K. S., Gordon, R. M. and Coale, K. H.: What controls dissolved iron concentrations
616 in the world ocean? *Mar. Chem.*, 57, 137-161, 1997.

617 King, B. et al.: Buoyancy frequency profiles and internal semidiurnal tide turning depths in the
618 oceans, *J. Geophys. Res.*, 117, C04008, 2012, doi:10.1029/2011JC007681.

619 Klunder, M. B., Laan, P., Middag, R., De Baar, H. J. W. and van Ooijen, J. C.: Dissolved iron
620 in the Southern Ocean (Atlantic sector), *Deep-Sea Res. II*, 58, 2678-2694, 2011.

621 Kunze, E., Firing, E., Hummon, J. M., Chereskin, T. K. and Thurnherr, A. M.: Global
622 abyssal mixing inferred from lowered ADCP shear and CTD strain profiles, *J. Phys.*
623 *Oceanogr.* 36, 1553-1576, 2006.

624 Larson, N., Pedersen, A. M.: Temperature measurements in flowing water: viscous heating
625 of sensor tips, Proc. 1st IGHEM Meeting, Montreal, PQ, Canada. [Available online at
626 http://www.seabird.com/technical_references/viscous.htm], 1996.

627 LeBlond, P. H. and Mysak, L. A.: *Waves in the Ocean*, Elsevier, Amsterdam NL, 602 pp, 1978.

628 Lueck, R. G.: Thermal inertia of conductivity cells: Theory, *J. Atmos. Oc. Technol.*, 7, 741-
629 755, 1990.

630 Mater, B. D., Venayagamoorthy, S. K., St. Laurent, L. and Moum, J. N.: Biases in Thorpe-scale
631 estimates of turbulence dissipation. Part I: Assessments from largescale overturns in
632 oceanographic data, *J. Phys. Oceanogr.*, 45, 2497-2521, 2015.

633 Martin A. P., et al.: The supply of nutrients due to vertical turbulent mixing: A study at the
634 Porcupine abyssal plain study site in the northeast Atlantic, *Deep-Sea Res. II*, 57, 1293-
635 1302, 2010.

636 Mensah, V., Le Menn, M. and Morel, Y.: Thermal mass correction for the evaluation of salinity,
637 *J. Atmos. Oc. Tech.*, 26, 665-672, 2009.

638 Middag, R., de Baar, H. J. W., Laan, P. and Bakker, K.: Dissolved aluminium and the silicon
639 cycle in the Arctic Ocean, *Marine Chemistry*, 115, 176-195, 2009.

640 Mojica, K. D. A. et al.: Phytoplankton community structure in relation to vertical stratification
641 along a north-south gradient in the Northeast Atlantic Ocean, *Limnol. Oceanogr.*, 60, 1498-
642 1521, 2015.

643 Mojica, K. D. A., Huisman, J., Wilhelm, S. W. and Brussaard, C. P. D.: Latitudinal variation
644 in virus-induced mortality of phytoplankton across the North Atlantic Ocean, *ISME J.*, 10,
645 500-513, 2016.

646 Moum, J. N. and Rippeth, T. P.: Do observations adequately resolve the natural variability of
647 oceanic turbulence?, *J. Mar. Sys.*, 77, 409-417, 2009.

648 Murphy, J. and Riley, J. P.: A modified single solution method for the determination of
649 phosphate in natural waters, *Anal. Chim. Acta*, 27, 31-36, 1962.

650 Oakey, N. S.: Determination of the rate of dissipation of turbulent energy from simultaneous
651 temperature and velocity shear microstructure measurements, *J. Phys. Oceanogr.*, 12, 256-
652 271, 1982.

653 Osborn, T. R.: Estimates of the local rate of vertical diffusion from dissipation measurements,
654 *J. Phys. Oceanogr.*, 10, 83-89, 1980.

655 Pearson, B. and Fox-Kemper, B.: Log-normal turbulence dissipation in global ocean models,
656 *Phys. Rev. Lett.*, 120, 094501, 2018.

657 Portwood, G. D., de Bruyn Kops, S. M. and Caulfield, C. P.: Asymptotic dynamics of high
658 dynamic range stratified turbulence, *Phys. Rev. Lett.*, 122, 194504, 2019.

659 Rijkenberg, M. J. A. et al.: Fluxes and distribution of dissolved iron in the eastern (sub-) tropical
660 North Atlantic Ocean, *Glob. Biogeochem. Cycl.*, 26, GB3004,
661 doi:10.1029/2011GB004264, 2012.

662 Rijkenberg, M. J. A. et al.: "PRISTINE", a new high volume sampler for ultraclean sampling
663 of trace metals and isotopes, *Mar. Chem.*, 177, 501-509, 2015.

664 Sarmiento, J. L. et al.: Response of ocean ecosystems to climate warming, *Glob. Biogeochem.*
665 *Cycl.*, 18, doi:10.1029/2003GB002134, 2004.

666 Scotti, A.: Biases in Thorpe-scale estimates of turbulence dissipation. Part II: energetics
667 arguments and turbulence simulations, *J. Phys. Oceanogr.*, 45, 2522-2543, 2015.

668 Sea-Bird: Fundamentals of the TC duct and pump-controlled flow used on Sea-Bird CTDs,
669 *Proc. Sea-Bird Electronics Appl. note 38*, SBE, Bellevue, WA, USA, 5 pp, 2012.

670 Smith, W. H. F. and Sandwell, D. T. : Global seafloor topography from satellite altimetry and
671 ship depth soundings, *Science* 277, 1957-1962, 1997.

672 Stansfield, K., Garrett, C., Dewey, R.: The probability distribution of the Thorpe displacement
673 within overturns in Juan de Fuca Strait, *J. Phys. Oceanogr.*, 31, 3421-3434, 2001.

674 Strickland, J. D. H. and Parsons, T. R.: A practical handbook of seawater analysis, First
675 edition, Fisheries Research Board of Canada, Bulletin, 167, 293 pp, 1968.

676 Thorpe, S. A.: Turbulence and mixing in a Scottish loch, *Phil. Trans. Roy. Soc. Lond. A*, 286,
677 125-181, 1977.

678 van Haren, H.: Tidal and near-inertial peak variations around the diurnal critical latitude,
679 *Geophys. Res. Lett.*, 32, L23611, doi:10.1029/2005GL024160, 2005.

680 van Haren, H.: Inertial and tidal shear variability above Reykjanes Ridge, *Deep-Sea Res. I*, 54,
681 856-870, 2007.

682 van Haren, H. and Gostiaux, L.: Characterizing turbulent overturns in CTD-data, *Dyn. Atmos.*
683 *Oc.*, 66, 58-76, 2014.

684 van Haren, H. and Laan, M.: An in-situ experiment identifying flow effects on temperature
685 measurements using a pumped CTD in weakly stratified waters, *Deep-Sea Res. I*, 111, 11-
686 15, 2016.

687 van Haren, H., Maas, L., Zimmerman, J. T. F., Ridderinkhof, H. and Malschaert, H.: Strong
688 inertial currents and marginal internal wave stability in the central North Sea, *Geophys.*
689 *Res. Lett.*, 26, 2993-2996, 1999.

690 Walter, M., Mertens, C. and Rhein, M.: Mixing estimates from a large-scale hydrographic
691 survey in the North Atlantic, *Geophys. Res. Lett.*, 32, L13605, doi:10.1029/2005GL022471,
692 2005.

693 Yamazaki, H. and Lueck, R.: Why oceanic dissipation rates are not lognormal, *J. Phys.*
694 *Oceanogr.*, 20, 1907-1918, 1990.

695

696

697 **Figure 1.** Bathymetry map of the Northeast Atlantic Ocean based on the 9.1 ETOPO-1 version
698 of satellite altimetry-derived data by Smith and Sandwell (1997). The numbered circles
699 indicate the CTD stations, at station 17 (x) no turbulence parameter, only nutrient sampling
700 was done. At stations 1 and 2 no DFe-samples were taken, at station 18 no nutrient-samples
701 were taken. Depth contours are at 2500 and 5000 m.

702

703 **Figure 2.** Test of effective removal of ship motions in CTD-data after pump in- and outlet
704 modification. Nearly raw 24 Hz sampled downcast data obtained from northern station 32
705 (cast 9). Short example time series for the 20-m depth range [10, 30] m. (a) Detrended
706 pressure (blue) and its (negative signed) first time derivative $-dp/dt$, 2-dbar-smoothed
707 (purple). (b) Detrended temperature. (c) Moderately smoothed (~ 30 degrees of freedom;
708 dof) spectra of data from the 5 to 500 m depth range. (d) Moderately smoothed (40 dof)
709 coherence between dp/dt and T from c., with dashed line indicating the 95% significance
710 level. (e) Corresponding phase difference.

711

712 **Figure 3.** Upper 500 m of turbulence characteristics computed from downcast density anomaly
713 data applying a threshold of $7 \times 10^{-5} \text{ kg m}^{-3}$. Northern station 29, cast 2. (a) Unordered, ‘raw’
714 profile of density anomaly referenced to the surface. (b) Overturn displacements following
715 reordering of the profiles in a. Slopes $\frac{1}{2}$ (solid lines) and 1 (dashed lines) are indicated. (c)
716 Logarithm of dissipation rate computed from the profiles in a., r.m.s. calculated over 7 m
717 intervals. We use the mathematics expression ‘lg’ for the 10-base logarithm, as given in
718 the ISO 80000 specification. (d) As c., but for eddy diffusivity. (e) Logarithm of buoyancy
719 frequency computed after reordering the profiles of a.

720

721 **Figure 4.** As Fig. 3, but for a southern station. Upper 500 m of turbulence characteristics
722 computed from downcast density anomaly data applying a threshold of $7 \times 10^{-5} \text{ kg m}^{-3}$.
723 Southern station 3, cast 4. (a) Unordered, ‘raw’ profile of density anomaly referenced to
724 the surface. (b) Overturn displacements following reordering of the profiles in a. Slopes $\frac{1}{2}$

725 (solid lines) and 1 (dashed lines) are indicated. (c) Logarithm of dissipation rate computed
726 from the profiles in a., r.m.s. calculated over 7 m intervals. (d) As c., but for eddy
727 diffusivity. (e) Logarithm of buoyancy frequency computed after reordering the profiles of
728 a.

729

730 **Figure 5.** Summer 2017 latitudinal transect along $17\pm 5^\circ\text{W}$ of turbulence values for upper 15 m
731 averages (green) and averages between $-100 < z < -25$ m (blue, seasonal pycnocline) and -
732 $500 < z < -100$ m (black, more permanent pycnocline) from short yoyos of 3 to 6 CTD-
733 casts. Values are given per cast (o) and station average (heavy circle with x; the size
734 corresponds with \pm the standard error for turbulence parameters). (a) Logarithm of
735 dissipation rate. (b) Logarithm of diffusivity. (c) Logarithm of buoyancy frequency (the
736 small symbols have the size of \pm the standard error). (d) Hour of sampling after sunrise.

737

738 **Figure 6.** Upper 500 m profiles for stations at three latitudes. (a) Density anomaly referenced
739 to the surface, including profiles from Fig. 3a and 4a. (b) Nitrate plus nitrite. (c) Phosphate.
740 (d) Silicate. (e) Dissolved iron.

741

742 **Figure 7.** Latitudinal transect of near-surface layers and wind conditions measured at stations
743 during the observational survey. (a) Mixed layer depth (x) and euphotic zone (o). (b) Wind
744 speed. (c) Wind direction.

745

746 **Figure 8.** Latitudinal transect of near-surface nutrient concentrations. (a) Dissolved iron
747 measured at depths indicated. Missing values reflect not all depths were sampled. (b)
748 Nitrate plus nitrite (red) and phosphate (blue, scale times 10) measured at depths indicated
749 in a. (c) Logarithm of (very weak within standard deviations of measurements) vertical
750 gradients of dissolved iron in a. (o-red) and phosphate in b. (x-blue). Only downgradient
751 values are shown, which excludes several PO_4^- and nearly all DFe-gradient values due to
752 near-surface increased values (*cf.* Fig. 6e, 32°N profile). (d). Upward vertical turbulent

753 fluxes of phosphate concentration gradients in c. using average surface K_z from Fig. 5b,
754 valid for depth average (here, ~17 m) of depths in a.

755

756 **Figure 9.** As Fig. 8, but for $-100 < z < -25$ m, with fluxes for ~62 m in d.

757

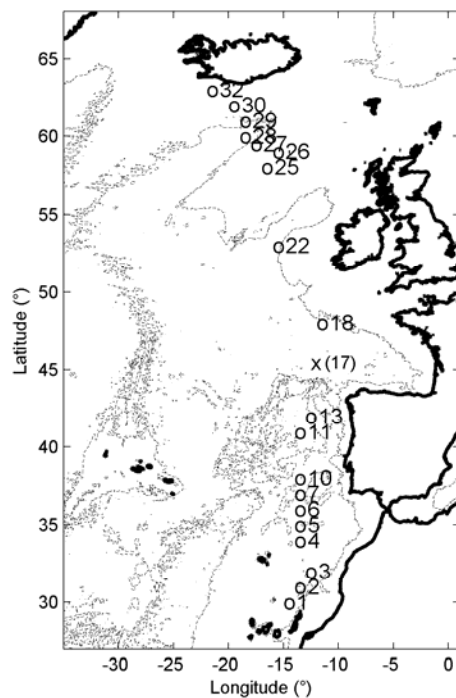
758 **Figure 10.** As Fig. 8, but for -600 (few nutrients sampled at 500) $< z < -100$ m, with fluxes for
759 ~350 m in d.

760

761 **Fig. A1.** SBE911 CTD-pump in- and outlet modification following the findings in van Haren
762 and Laan (2016). (a) The T- and C-sensors clamped together with a structure holding in-
763 and outlet pump-tubing of exactly the same diameter, separated at 0.3 m distance in the
764 horizontal plane. (b) The modification of a. mounted in the CTD-frame.

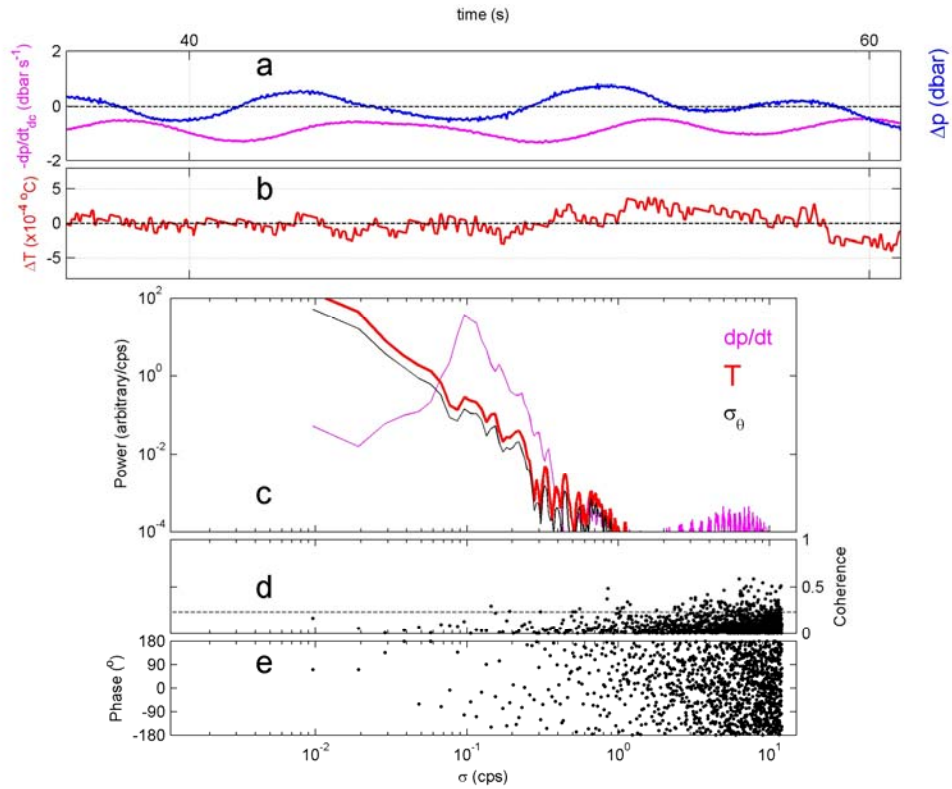
765

766 **Fig. A2.** Probability Density Functions of logarithm of vertically averaged dissipation rate in
767 comparison with latitudinal trend extreme values. (a) Distribution as a function of latitude
768 for all data. (b) As a, but for the upper 15 m averages only. The mean value is given by the
769 vertical purple line, with the horizontal line indicating +/- 1 standard deviation. The vertical
770 light-blue lines indicate the best-fit value of the trend for 30° and 63°N. (c) As b, but for
771 averages between $-100 < z < -25$ m. (d) As c, but for averages between $-500 < z < -100$ m.



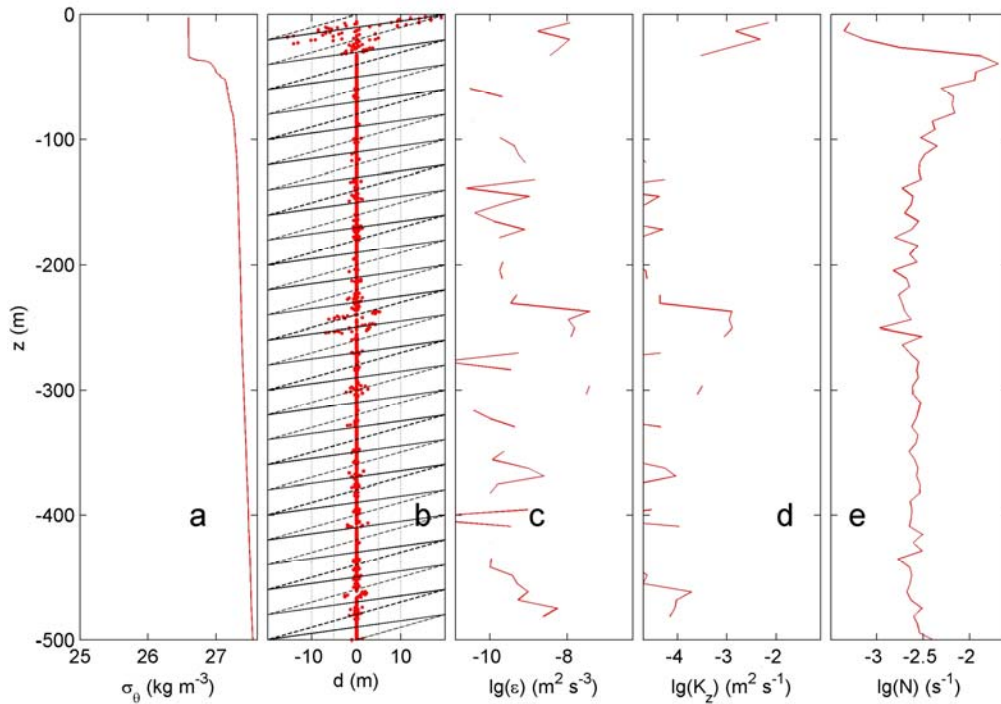
772
 773
 774
 775
 776
 777
 778

Figure 1. Bathymetry map of the Northeast Atlantic Ocean based on the 9.1 ETOPO-1 version of satellite altimetry-derived data by Smith and Sandwell (1997). The numbered circles indicate the CTD stations, at station 17 (x) no turbulence parameter, only nutrient sampling was done. At stations 1 and 2 no DFe-samples were taken, at station 18 no nutrient-samples were taken. Depth contours are at 2500 and 5000 m.



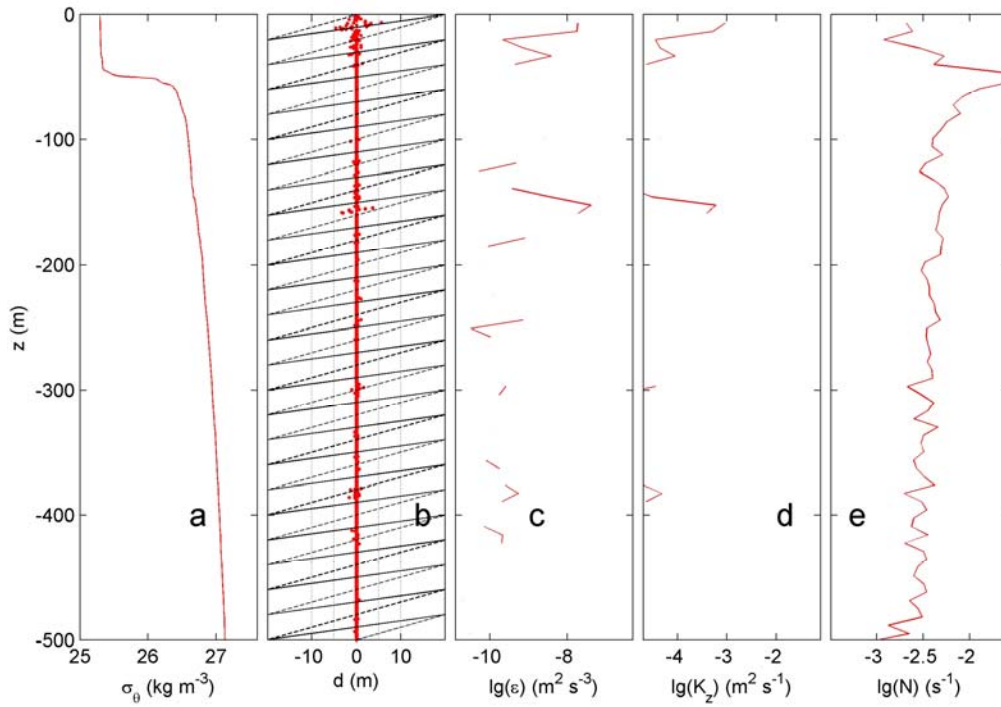
780
 781
 782
 783
 784
 785
 786
 787
 788
 789

Figure 2. Test of effective removal of ship motions in CTD-data after pump in- and outlet modification. Nearly raw 24 Hz sampled downcast data obtained from northern station 32 (cast 9). Short example time series for the 20-m depth range [10, 30] m. (a) Detrended pressure (blue) and its (negative signed) first time derivative $-dp/dt$, 2-dbar-smoothed (purple). (b) Detrended temperature. (c) Moderately smoothed (~ 30 degrees of freedom; dof) spectra of data from the 5 to 500 m depth range. (d) Moderately smoothed (40 dof) coherence between dp/dt and T from c., with dashed line indicating the 95% significance level. (e) Corresponding phase difference.



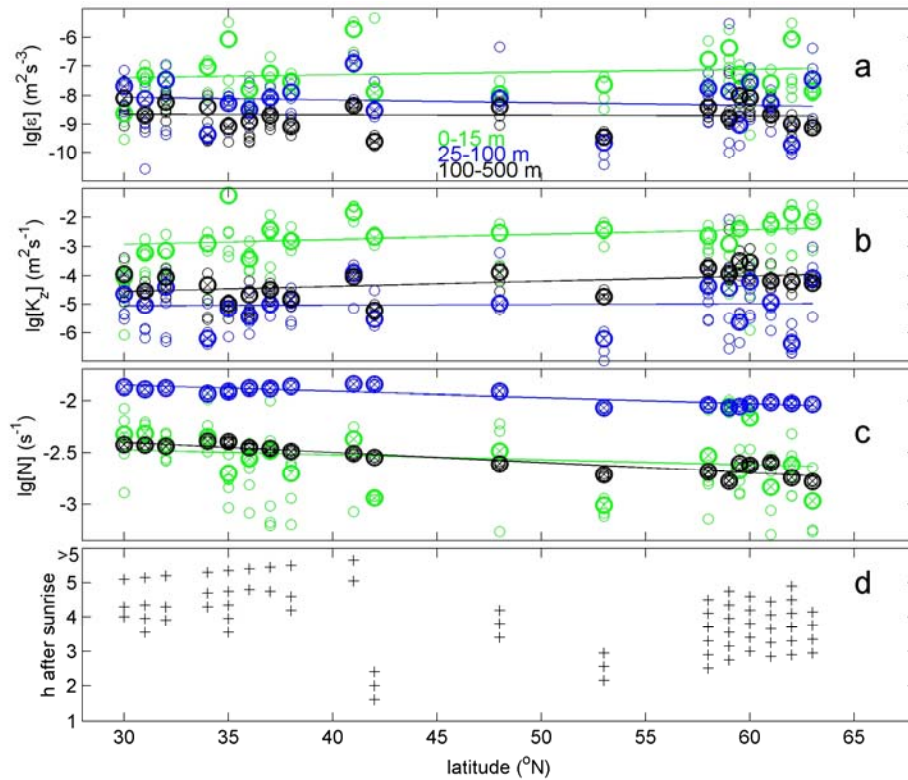
790
791
792
793
794
795
796
797
798
799
800

Figure 3. Upper 500 m of turbulence characteristics computed from downcast density anomaly data applying a threshold of $7 \times 10^{-5} \text{ kg m}^{-3}$. Northern station 29, cast 2. (a) Unordered, ‘raw’ profile of density anomaly referenced to the surface. (b) Overturn displacements following reordering of the profiles in a. Slopes $\frac{1}{2}$ (solid lines) and 1 (dashed lines) are indicated. (c) Logarithm of dissipation rate computed from the profiles in a., r.m.s. calculated over 7 m intervals. We use the mathematics expression ‘lg’ for the 10-base logarithm, as given in the ISO 80000 specification. (d) As c., but for eddy diffusivity. (e) Logarithm of buoyancy frequency computed after reordering the profiles of a.



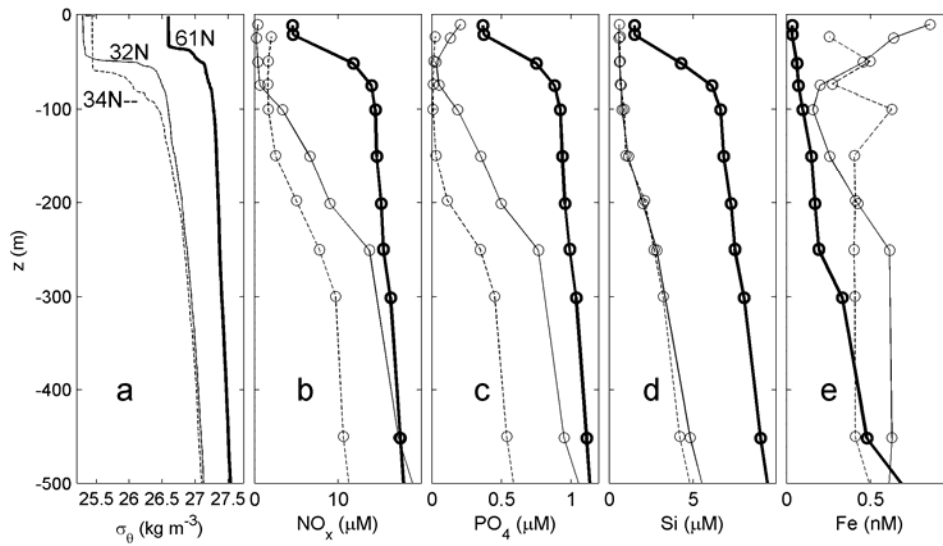
801
 802
 803
 804
 805
 806
 807
 808
 809
 810

Figure 4. As Fig. 3, but for a southern station. Upper 500 m of turbulence characteristics computed from downcast density anomaly data applying a threshold of $7 \times 10^{-5} \text{ kg m}^{-3}$. Southern station 3, cast 4. (a) Unordered, ‘raw’ profile of density anomaly referenced to the surface. (b) Overturn displacements following reordering of the profiles in a. Slopes $\frac{1}{2}$ (solid lines) and 1 (dashed lines) are indicated. (c) Logarithm of dissipation rate computed from the profiles in a., r.m.s. calculated over 7 m intervals. (d) As c., but for eddy diffusivity. (e) Logarithm of buoyancy frequency computed after reordering the profiles of a.



811
 812
 813
 814
 815
 816
 817
 818
 819

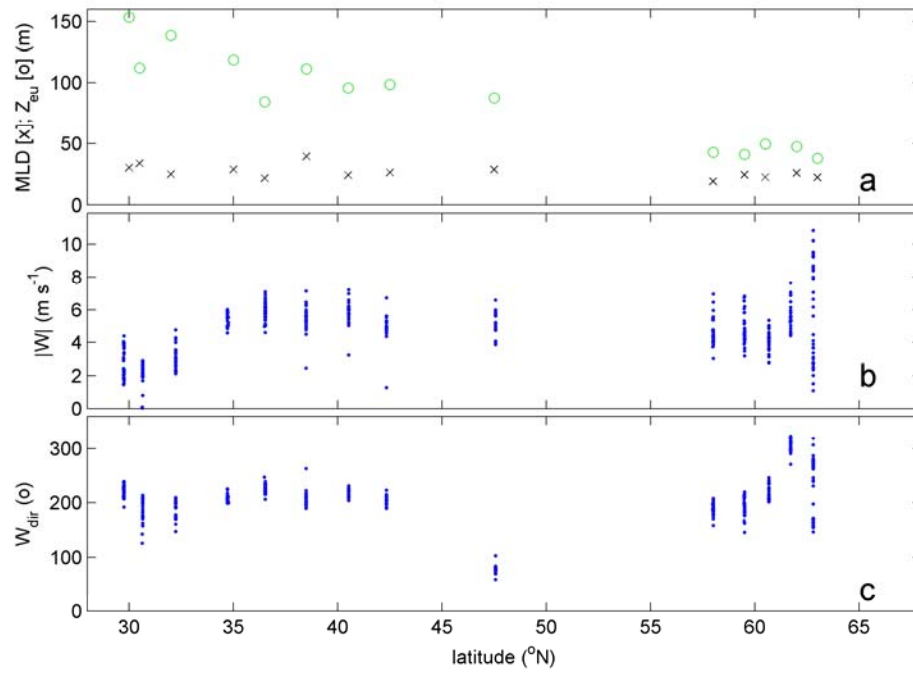
Figure 5. Summer 2017 latitudinal transect along $17\pm 5^\circ\text{W}$ of turbulence values for upper 15 m averages (green) and averages between $-100 < z < -25$ m (blue, seasonal pycnocline) and $-500 < z < -100$ m (black, more permanent pycnocline) from short yoyos of 3 to 6 CTD-casts. Values are given per cast (o) and station average (heavy circle with x; the size corresponds with \pm the standard error for turbulence parameters). (a) Logarithm of dissipation rate. (b) Logarithm of diffusivity. (c) Logarithm of buoyancy frequency (the small symbols have the size of \pm the standard error). (d) Hour of sampling after sunrise.



820
 821
 822
 823
 824

Figure 6. Upper 500 m profiles for stations at three latitudes. (a) Density anomaly referenced to the surface, including profiles from Fig. 3a and 4a. (b) Nitrate plus nitrite. (c) Phosphate. (d) Silicate. (e) Dissolved iron.

825



826

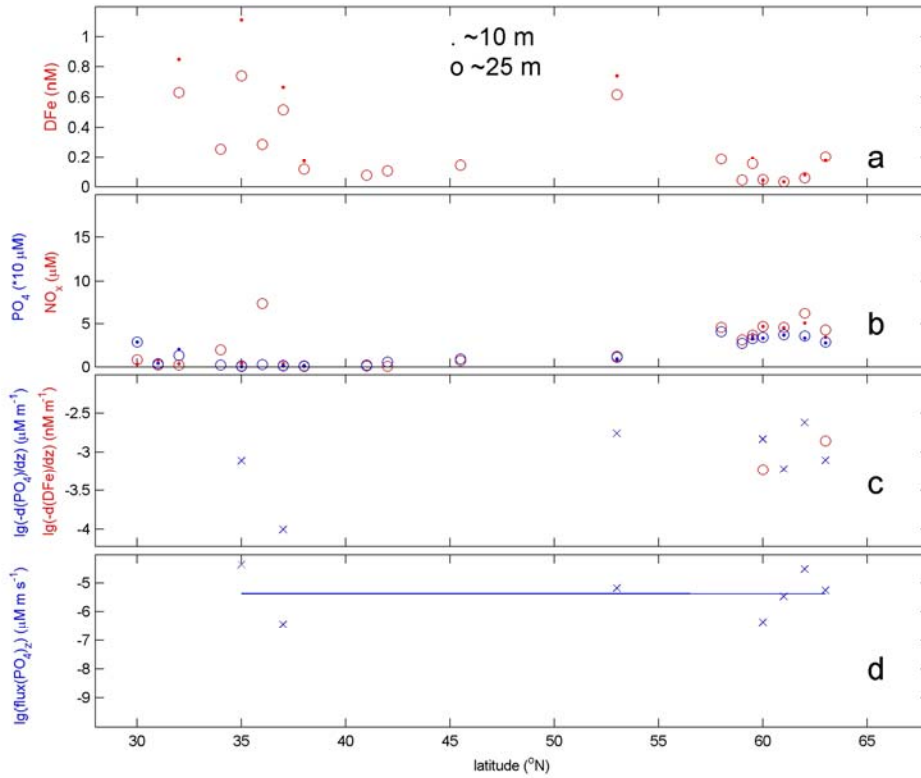
827

828

829

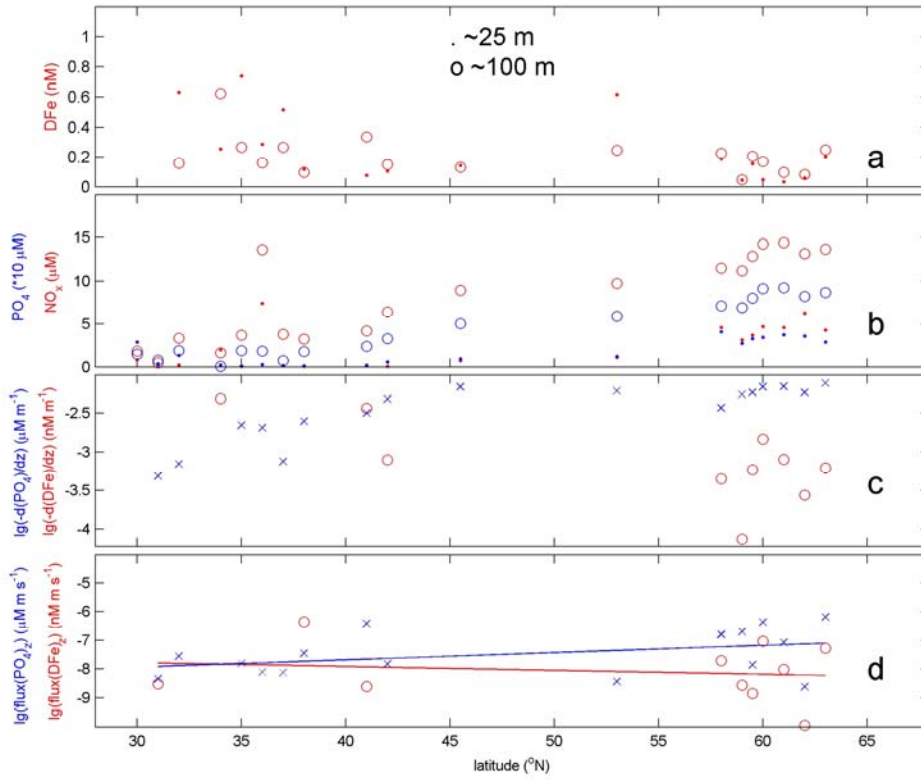
830

Figure 7. Latitudinal transect of near-surface layers and wind conditions measured at stations during the observational survey. (a) Mixed layer depth (x) and euphotic zone (o). (b) Wind speed. (c) Wind direction.



831
 832
 833
 834
 835
 836
 837
 838
 839
 840
 841

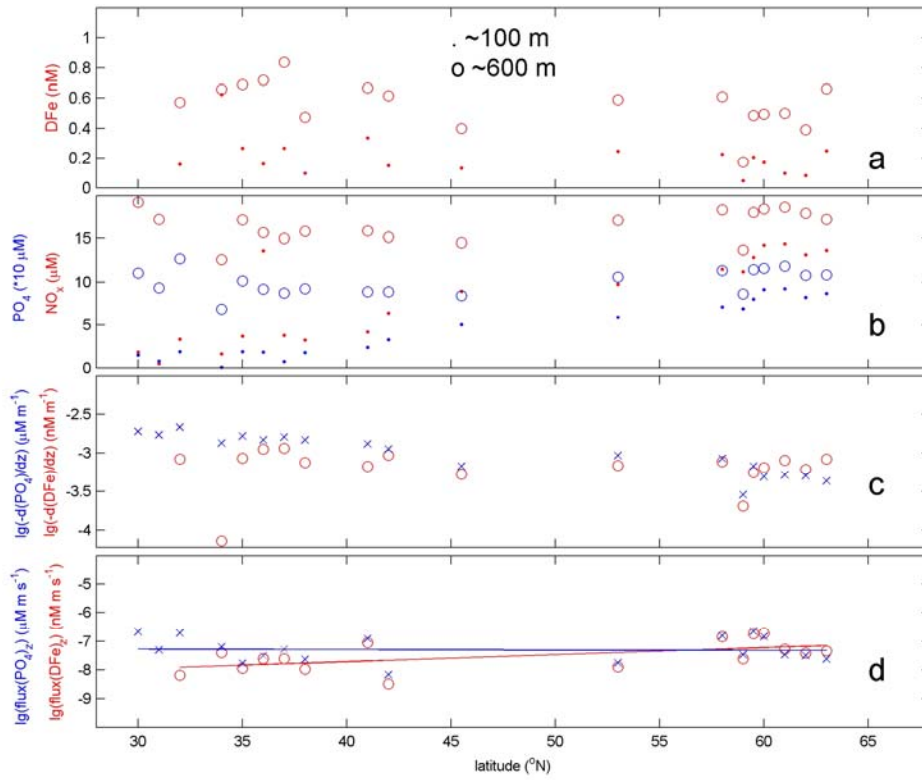
Figure 8. Latitudinal transect of near-surface nutrient concentrations. (a) Dissolved iron measured at depths indicated. Missing values reflect not all depths were sampled. (b) Nitrate plus nitrite (red) and phosphate (blue, scale times 10) measured at the depths indicated in a. (c) Logarithm of (very weak within standard deviations of measurements) vertical gradients of dissolved iron in a. (o-red) and phosphate in b. (x-blue). Only downgradient values are shown, which excludes several PO_4^- - and nearly all DFe-gradient values due to near-surface increased values (*cf.* Fig. 6e, 32°N profile). (d). Upward vertical turbulent fluxes of phosphate concentration gradients in c. using average surface K_z from Fig. 5b, valid for the depth average (here, ~ 17 m) of depths in a.



842
843
844

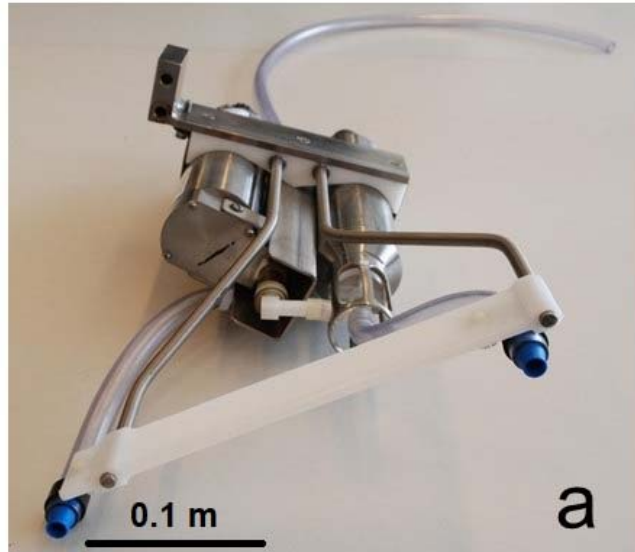
Figure 9. As Fig. 8, but for $-100 < z < -25$ m, with fluxes for ~ 62 m in d.

845



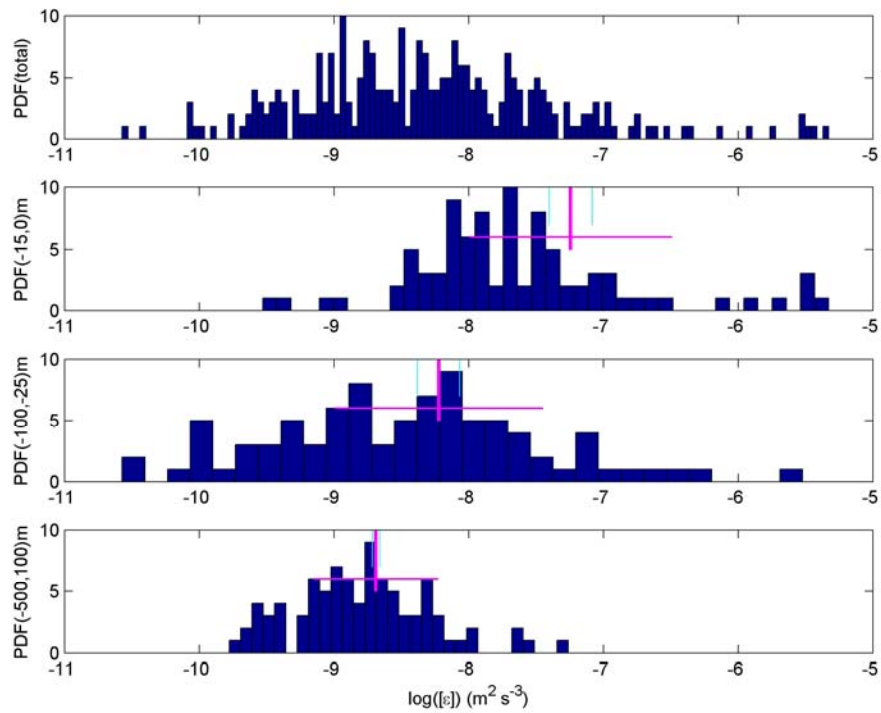
846
847
848
849

Figure 10. As Fig. 8, but for -600 (few nutrients sampled at 500) $< z < -100$ m, with fluxes for ~ 350 m in d.



850
851
852
853
854
855

Fig. A1. SBE911 CTD-pump in- and outlet modification following the findings in van Haren and Laan (2016). (a) The T- and C-sensors clamped together with a structure holding in- and outlet pump-tubing of exactly the same diameter, separated at 0.3 m distance in the horizontal plane. (b) The modification of a. mounted in the CTD-frame.



856

857

858

859

860

861

862

863

864

865

866

Fig. A2. Probability Density Functions of logarithm of vertically averaged dissipation rate in comparison with latitudinal trend extreme values. (a) Distribution as a function of latitude for all data. (b) As a, but for the upper 15 m averages only. The mean value is given by the vertical purple line, with the horizontal line indicating ± 1 standard deviation. The vertical light-blue lines indicate the best-fit value of the trend for 30° and 63°N . (c) As b, but for averages between $-100 < z < -25$ m. (d) As c, but for averages between $-500 < z < -100$ m.